## Characterization

Gel permeation chromatography (GPC, 2414, Waters, USA) was employed for analysis, using chromatographically pure N,N-dimethylformamide (DMF) as the mobile phase at a flow rate of 0.4 mL/min. The column temperature was maintained at 40°C, and the refractive index (RI) detector temperature was set at 45°C. The chemical composition of the samples was determined by X-ray photoelectron spectroscopy (XPS, AXIS Ultra DLD, Kratos, UK). The crosslinking density of the samples was characterized using low-field nuclear magnetic resonance (LF-NMR, PQ001, Niumag Analytical Instrument Co., Suzhou, China), with the sample height fixed at approximately 1 cm and the testing temperature set to 90°C. X-ray diffraction (XRD, D8 Advance, Bruker, Germany) measurements were performed using Cu Kα radiation (λ = 0.15405 nm) with a scanning rate of $0.02°\cdot s^{-1}$ over a scanning angle (2θ) range of 5° to 70°. The self-healing efficiency was evaluated according to the method proposed by Wool and O'Connor, which is widely adopted as the standard for quantifying "self-healing efficiency" in self-healing systems[1,2]. The calculation formula for the self-healing efficiency is given by Equation (S1):

$$\eta = \frac{\sigma_{healed}}{\sigma_{virgin}} \times 100\% \tag{S1}$$

$\sigma_{virgin}$ —— Tensile strength of the pristine specimen /MPa；

$\sigma_{healed}$ —— Tensile strength of the healed specimen /MPa。

## GPC Characterization of Se-E51 and Se-EP

Comparative analysis between Se-EP and Se-E51 revealed that Se-EP exhibits a markedly higher molecular weight. This significant difference indicates the successful synthesis of Se-EP with an increased molecular weight based on the structure of Se-E51. Additionally, both materials show polydispersity index (PDI) values close to 1, suggesting a narrow molecular weight distribution, relatively uniform polymer chain lengths, and no significant polydispersity.

**Table S1 Molecular weight distribution of Se-E51 and Se-EP**

| Samples | Retention time (min) | $M_n$ (g·mol$^{-1}$) | $M_w$ (g·mol$^{-1}$) | PDI |
|---|---|---|---|---|
| Se-E51 | 19.10 | 48708 | 48777 | 1.001 |
| Se-EP | 17.48 | 51256 | 51507 | 1.005 |

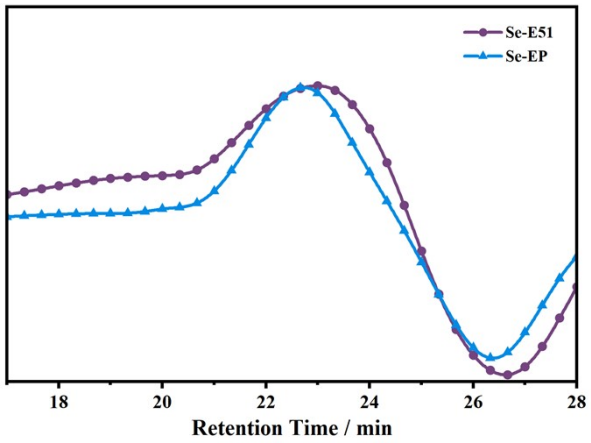


**Fig. S1 GPC curves of Se-E51 and Se-EP**

## NMR Characterization of DiSe-DiOH

In Fig. S2a, the signal at 3.01 ppm (2H, t) is assigned to H-a, 3.64 ppm (2H, m) is assigned to H-b, and 4.92 ppm (1H, s) is assigned to H-c. Additionally, 3.36 ppm corresponds to the water signal. In Fig. S2b, the signal at 32.73 ppm is attributed to C-a, and 61.27 ppm is attributed to C-b. Based on the combined results of $^{1}$H NMR, $^{13}$C NMR, and FT-IR, it can be concluded that DiSe-DiOH has been successfully synthesized[3].

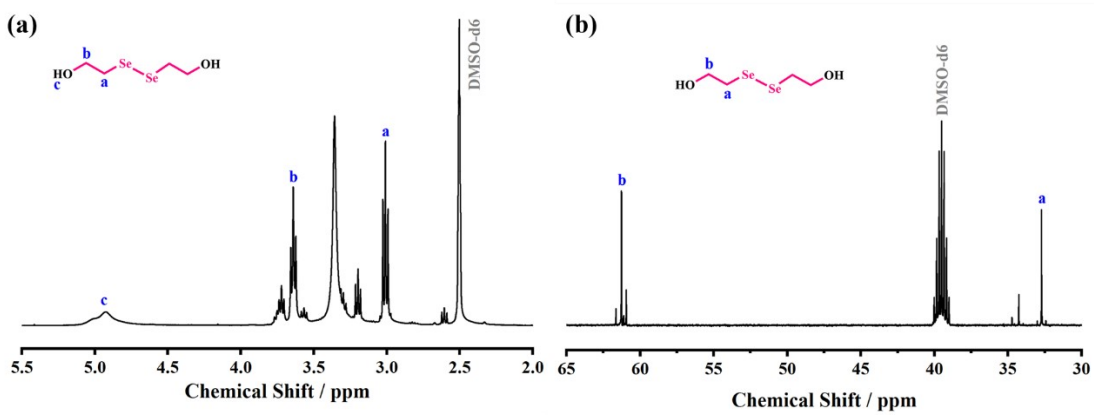

**Fig. S2 (a) $^{1}$H-NMR of DiSe-DiOH; (b) $^{13}$C-NMR of DiSe-DiOH (all solvents were DMSO-$d_6$)**

## XPS Characterization of MXene

In the C 1s spectrum (Fig. S3b), three peaks are observed at 281.9, 284.8, and 288.3 eV, which correspond to C–Ti, C–C, and C–O bonds, respectively. In the O 1s spectrum (Fig. S3c), three peaks appear at 529.7, 531.6, and 533.2 eV, assigned to lattice oxygen, C–Ti–O, and adsorbed water, respectively. The F 1s spectrum (Fig. S3d) is dominated by a peak at 684.7 eV attributed to F–Ti, along with an additional peak at 685.8 eV arising from residual metal fluorides resulting from the etching process. In the Ti 2p spectrum (Fig. S3e), two characteristic peaks corresponding to Ti–C and Ti–O are identified.

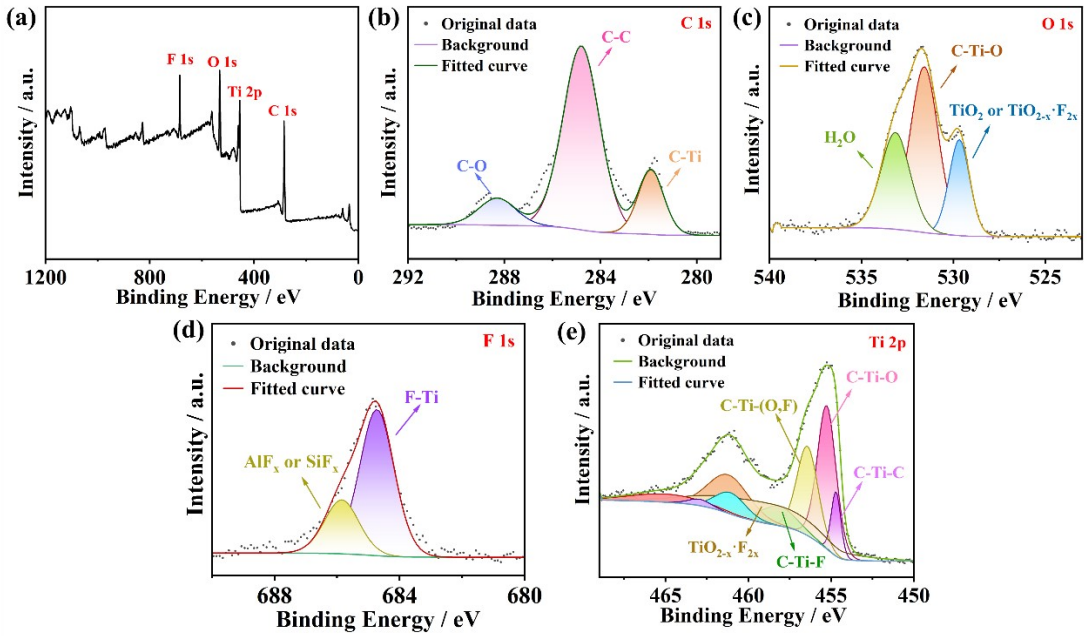


**Fig. S3 XPS spectra of MXene: (a) Survey spectra, (b) C 1s, (c) O 1s, (d) F 1s, (e) Ti 2p**

## SEM and TEM Characterization of MXene

As shown in Fig. S4 (a-e), the results indicate that MXene exhibits a typical multilayered stacked nanosheet structure with an accordion-like morphology, and the observations from SEM and TEM are consistent with each other. Furthermore, elemental mapping in Fig. S4f reveals a uniform distribution of Ti, F, and O elements

across the MXene. Combined with XPS analysis, it can be inferred that F and O correspond to the surface functional groups –OH and –F on MXene[4,5].

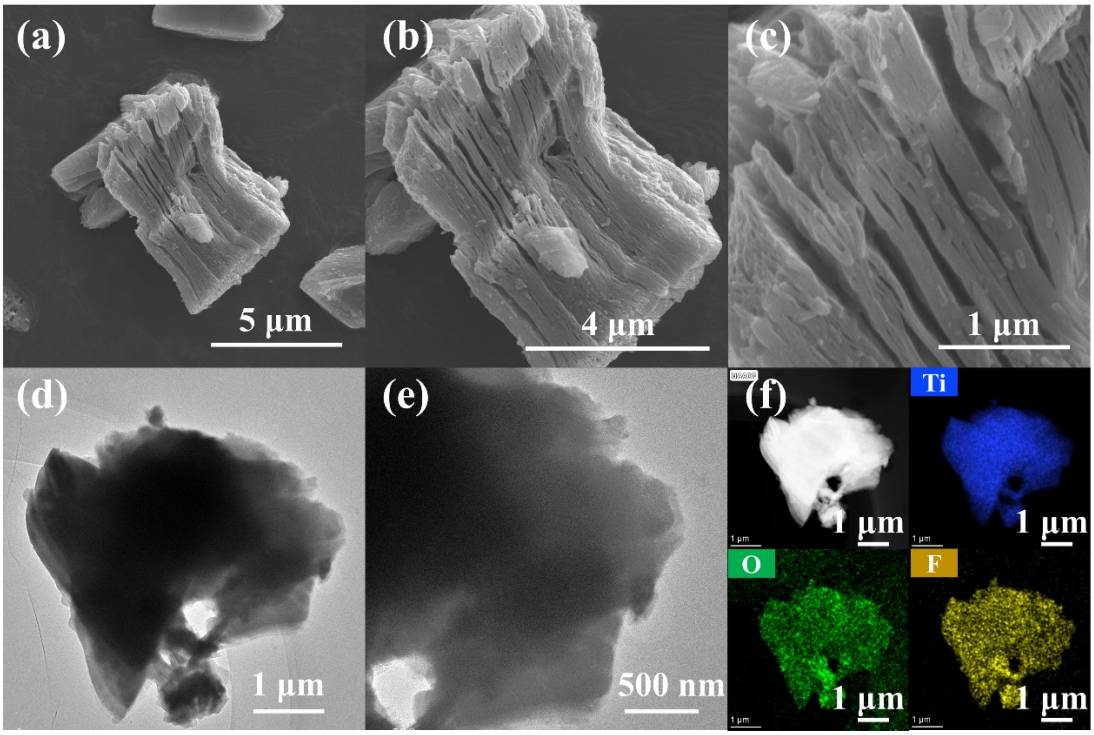


**Fig. S4 (a-c) SEM images of MXene; (d-e) TEM images of MXene; (f) Element mapping of MXene**

## TGA Characterization of Se-EP and MXene/Se-EP

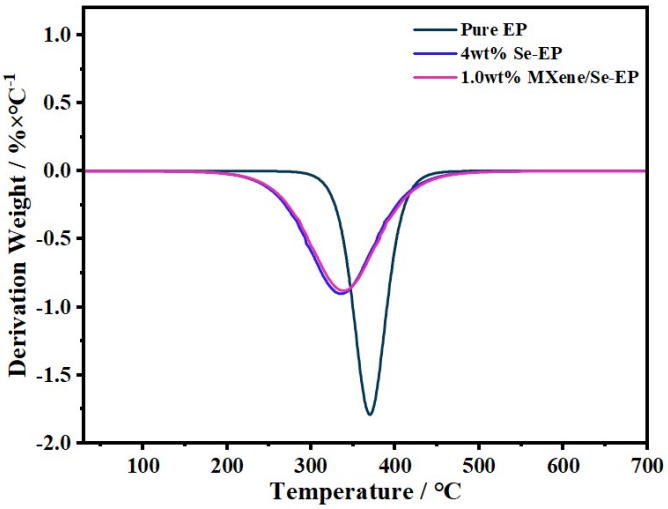


**Fig. S5 DTG curves of 4.0 wt% Se-EP and 1.0 wt% MXene/Se-EP**

**Table S2 Thermal decomposition temperature of 4.0 wt% Se-EP and 1.0 wt% MXene/Se-EP**

| Samples | $T_{5\%}$ (℃) | $T_{50\%}$ (℃) | Char yield (%) |
|---|---|---|---|
| Pure EP | 333.70 | 372.80 | 9.27 |
| 4.0 wt% Se-EP | 261.07 | 339.51 | 5.70 |
| 1.0 wt% MXene/Se-EP | 264.36 | 343.58 | 6.58 |

## XRD Characterization of Se-EP and MXene/Se-EP

In Fig. S6, the characteristic (002) peak of MXene observed at 2θ = 6.3° corresponds to MXene. Compared with 4.0 wt% Se-EP, the diffraction intensity of 1.0 wt% MXene/Se-EP in the range of 2θ = 19-24° is reduced. Therefore, combined with the results of DMA and the analysis of surface functional groups on MXene, the addition of 1.0 wt% MXene to the resin, in comparison with 4.0 wt% Se-EP, entails the formation of more hydrogen bonds near the crosslinking sites. This indicates stronger hydrogen-bond interactions in these regions, which restrict the movement of epoxy segments, reduce free volume, and consequently lead to an elevation of the Tg[6].

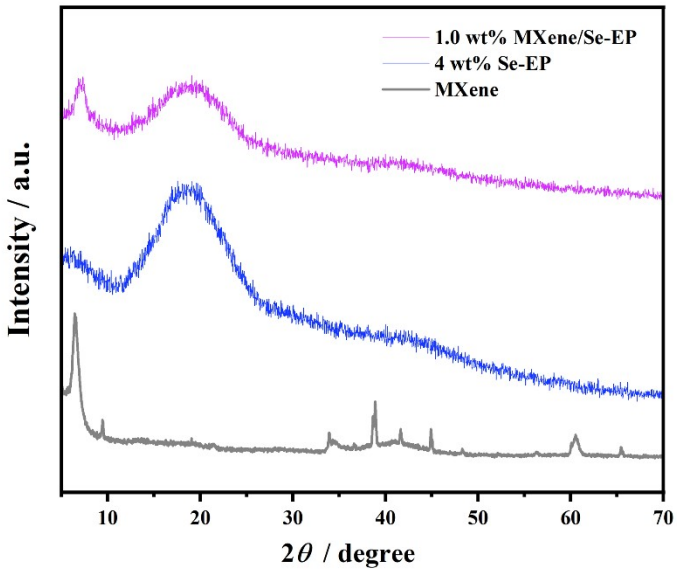


**Fig. S6 XRD spectra of 1.0 wt% MXene/Se-EP、4.0 wt% Se-EP and Mxene**

## Storage Modulus of Se-EP and MXene/Se-EP

In the vicinity of the glass transition temperature, the storage modulus decreases

sharply and then stabilizes, forming a plateau modulus. This phenomenon fully indicates that within the tested temperature range, the crosslinked network maintains stable connectivity. Furthermore, the initial storage modulus of the 1.0 wt% MXene/Se-EP curve is enhanced. This change is primarily attributed to the effective promotion of stress transfer from the epoxy resin to MXene by the introduced MXene, thereby improving the stability and load-bearing capacity of the material during application. Simultaneously, the abundant active functional groups on the surface of the MXene play a crucial role. They actively participate in the curing reaction of the epoxy resin, laying the foundation for the enhancement of material properties[7].

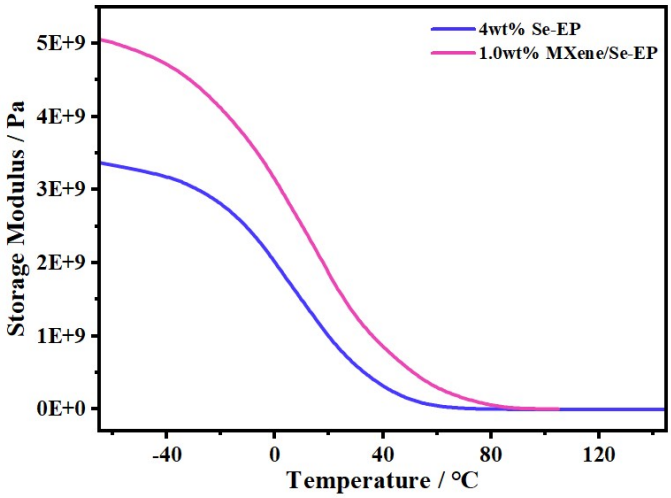


**Fig. S7 Storage modulus curves of 4.0 wt% Se-EP and 1.0 wt% MXene/Se-EP**

## Glass Transition Temperatures of Pure EP and MXene/Se-EP

The introduction of diselenide bonds led to a decrease in the Tg compared to pure EP. Although the incorporation of MXene partially restored thermal stability, its effect was limited due to the low loading. Nevertheless, the composite exhibited a Tg of 85.97°C, which indicates that it retains thermal stability.

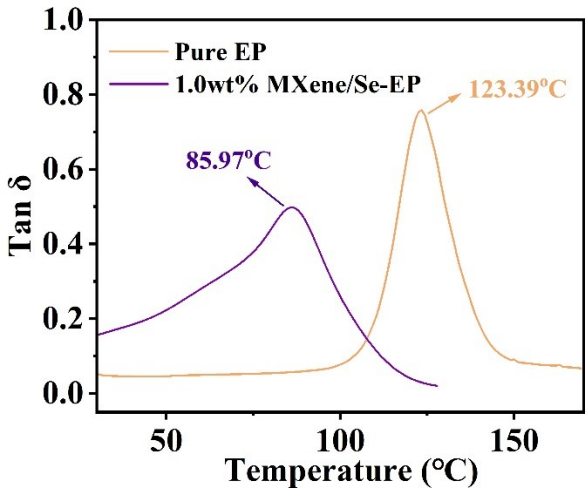


**Fig. S8 tan δ curves of Pure EP and 1.0 wt% MXene/Se-EP**

## Self-Healing Properties of Se-EP and MXene/Se-EP

**Table S3 Self-healing performance of 4.0 wt% Se-EP under different repair conditions**

| Samples | Stress (Mpa) | Strain (%) | Young's Modulus (Mpa) | Self-healing efficiency (%) |
|---|---|---|---|---|
| 4.0 wt% Se-EP | 9.71 | 97.50 | 79.43 | 0.0 |
| UV light for 2 h | 1.58 | 33.00 | 8.08 | 16.3 |
| UV light for 4 h | 3.46 | 35.37 | 15.12 | 35.7 |
| UV light for 6 h | 5.23 | 49.84 | 25.14 | 53.8 |
| Xenon lamp for 2 h | 2.24 | 18.31 | 20.98 | 23.0 |
| Xenon lamp for 4 h | 4.55 | 25.45 | 52.49 | 46.9 |
| Xenon lamp for 6 h | 7.42 | 23.97 | 76.74 | 76.4 |

**Table S4 Self-healing performance of 1.0 wt% MXene/Se-EP under xenon lamp**

| Samples | Stress (Mpa) | Strain (%) | Young's Modulus (Mpa) | Self-healing efficiency (%) |
|---|---|---|---|---|
| 1.0 wt% MXene/Se-EP | 22.07 | 71.82 | 276.47 | 0.0 |
| Xenon lamp for 2 h | 11.42 | 15.07 | 158.31 | 51.8 |
| Xenon lamp for 4 h | 16.80 | 55.01 | 198.94 | 76.1 |
| Xenon lamp for 6 h | 21.26 | 72.58 | 249.12 | 96.3 |

**Table S5 Cyclic Self-Healing Performance of 1.0 wt% MXene/Se-EP under Xenon Lamp**

| Samples | Stress (Mpa) | Strain (%) | Young's Modulus (Mpa) | Self-healing efficiency (%) |
|---|---|---|---|---|
| Self-repairing for the first time | 21.26 | 72.58 | 249.12 | 96.3 |
| Self-repairing for the second time | 10.73 | 52.21 | 210.12 | 48.6 |
| Self-repairing for the third time | 4.65 | 28.05 | 81.53 | 21.1 |

## References：


1 R. P. Wool and K. M. O’ Connor, Journal of Applied Physics, 1981, **52**, 5953-5963.

2 E. N. Brown, N. R. Sottos and S. R. White, Experimental Mechanics, 2002, **42**, 372-379.

3 We. Du, Y. Jin, J. Pan, W. Fan, S. Lai, X. Sun, Journal of Applied Polymer Science, 2018, **135**, 46326.

4 L. Wang, Z. Bai, X. Zhang and G. Li, ACS Applied Nano Materials, 2022, **5**, 9666-9677.

5 N. Liu, L. Yu, B. Liu, F. Yu, L. Li, Y. Xiao, J. Yang and J. Ma, Adv. Sci. 2023, **10**, 2204041.

6 R. Cai, J. Zhao, N. Lv, A. Fu, C. Yin, C. Song and M. Chao, Nanomaterials, 2022, **12**, 2249.

7 C. Yu, X. Li, X Yang, X. Qiu, X. Zhang, Z. Chen and Y. Luo, Small, 2024, **20**, 2311656.